# A Study of Keyhole Porosity in Selective Laser Melting: Single-Track Scanning With Micro-CT Analysis

**Subin Shrestha**[1]
J.B. Speed School of Engineering,
University of Louisville,
Louisville, KY 40292
e-mail: subin.shrestha@louisville.edu

**Thomas Starr**
J.B. Speed School of Engineering,
University of Louisville,
Louisville, KY 40292
e-mail: tom.starr@louisville.edu

**Kevin Chou**
J.B. Speed School of Engineering,
University of Louisville,
Louisville, KY 40292
e-mail: kevin.chou@louisville.edu

*Porosity is an inherent attribute in selective laser melting (SLM) and profoundly degrades the build part quality and its performance. This study attempts to understand and characterize the keyhole pores formed during single-track scanning in SLM. First, 24 single tracks were generated using different line energy density (LED) levels, ranging from 0.1 J/mm to 0.98 J/mm, by varying the laser power and the scanning speed. The samples were then scanned by micro-computed tomography to measure keyhole pores and analyze the pore characteristics. The results show a general trend that the severity of the keyhole porosity increases with the increase of the LED with exceptions of certain patterns, implying important individual contributions from the parameters. Next, by keeping the LED constant in another set of experiments, different combinations of the power and the speed were tested to investigate the individual effect. Based on the results obtained, the laser power appears to have a greater effect than the scanning speed on both the pore number and the pore volume as well as the pore depth. For the same LED, the pore number and volume increase with increasing laser power until a certain critical level, beyond which, both the pore number and volume will decrease, if the power is further increased. For the LED of 0.32 J/mm, 0.4 J/mm, and 0.48 J/mm, the critical laser power that reverses the trend is about 132 W, 140 W, and 144 W, respectively.* [DOI: 10.1115/1.4043622]

*Keywords: additive manufacturing, computed tomography, porosity, selective laser melting*

## 1 Introduction

Selective laser melting (SLM) is a metal-based additive manufacturing process that utilizes a laser to selectively melt powder particles and form the desired product after a layer-by-layer fabrication process [1]. SLM process has been applied to fabricate parts from different metallic materials such as aluminium [2,3], nickel [4,5], titanium [6,7], steel [8,9], etc. Among those, titanium alloy Ti-6Al-4 V has been favored in aerospace industries [10] as well as biomedical applications [11–13] due to its high specific strength and biocompatibility [14].

In spite of its freeform capability, the SLM process has issues of process-induced defects such as porosity, cracks, part deformation, etc. [15,16]. Pores formed during the process may be characterized as the keyhole pores and the lack of fusion pores [17]. These pores if present within the SLM parts would degrade its part performances [9,10,18] and therefore part optimization by porosity reduction is desired. Leuders et al. [18] explained that pores within SLM samples have a drastic effect on fatigue behavior and the significant extension of the crack initiation phase can be achieved by reducing the porosity.

Pore formation during the SLM process is affected by the energy density input, which is a function of the laser power, the scan speed, the hatch spacing, and the layer thickness. Gong et al. [19] investigated part quality based on different energy densities and demonstrated that the process window in SLM of Ti-6Al-4 V could be divided into three groups, insufficient melting, conduction melting, and keyhole melting. When the energy density is very high, the temperature within the melt pool exceeds the boiling point leading to material evaporation. The material evaporation would generate an

evaporation pressure, and the deep depression formed within the melt pool is known as a keyhole. Such a melting is known as keyhole mode melting [20]. As the energy density gets reduced, keyhole formation is not observed, and the mode of melting is called the conduction melting. If the energy density gets further reduced, partial melting occurs, which lead to balling behavior and discontinuity in the track formation.

A few investigations toward part porosity developed during the SLM process have been carried out. Ponnusamy et al. [21] performed a statistical analysis to investigate the effect of various process parameters such as laser power, layer thickness, etc. toward porosity. Besides, various studies have been conducted to characterize porosity using X-ray tomography methods. Slotwinski et al. [22] utilized X-ray computed tomography (XRCT) to measure porosity on additively manufactured cobalt-chrome (Co-Cr) samples. The XRCT technique can help determine the pore distribution within the sample as well as the pore morphology. However, the accuracy of the representation would depend on the resolution of the system. Similarly, Zhou et al. [23] used synchrotron radiation micro-CT to observe the defects formed within SLM parts. They concluded that such an imaging technique is a feasible method to obtain 3D images of SLM defects accurately. Furthermore, Ziółkowski et al. [24] explained the advantage of nondestructive XRCT over traditional metallographic cross-sectional analysis. Siddique et al. [25] used a voxel resolution of 4.8 $\mu$m to scan the SLM specimen. In addition, the authors performed a two-dimensional metallographic study to calculate the porosity, and the authors found that porosity calculated by metallographic studies and three-dimensional tomography had no significant difference considering the critical pores. Kim et al. [26] used X-ray microtomography to study the track changes in the morphology of SLM Ti porous structures at a different stage of post laser melting production. They have demonstrated that $\mu$CT can be used not only for 3D quantification but also as a feedback mechanism to make improvements on

---

initial designs. Van Bael et al. [27] used XRCT as a feedback mechanism to improve the geometrical and mechanical controllability of selective laser melted Ti-6Al-4 V porous structures. The mismatch between the designed and the measured properties such as pore size, strut thickness, strut volume, and porosity from the first run were integrated into the second run, which helped to minimize the mismatch.

Kasperovich et al. [17] presented the correlation between the process parameters and the porosity formation during SLM fabrication of Ti-6Al-4 V parts. The authors showed that two types of void defects were present in SLM parts and the optimization of the process parameters could reduce porosity volume fraction. Circular/spherical pores were formed with the excessive energy input, whereas insufficient energy density resulted in elongated, narrow crack-like voids. Besides, there are combinations of power, speed, etc. which would result in the same energy densities. Hence, energy density effect, as well as individual parameter effects, should be investigated to identify the process parameters which have more contributions toward porosity formation. In addition, it is also important to characterize the pores, as the pore location and pore size are critical to the stress concentration and pores near to the surface are more critical even if they are small in size [25].

The objective of this study is to understand the characteristics of the keyhole pores resulting from different process settings. The effect of power and speed on pore size distribution and pore depth is also a subject of interest. To achieve the objectives, single tracks with different energy densities are fabricated inside hollow cylindrical samples. The samples are scanned using a micro-CT ($\mu$CT) scanner, and the reconstructed images are analyzed. Keyhole pore characteristics such as pore size, pore volume, sphericity, etc. are obtained. Total pore number and pore volume of the pores formed within the single track are also measured. In addition to the energy density effect, the effect of power and speed toward keyhole porosity was investigated, by keeping energy density as constant.

# 2 Experimental Approach

## 2.1 SLM Specimen Design and Fabrications.
Figure 1(a) shows the design and dimensions of hollow semicylinders samples. The cylinder design is considered to minimize the artifacts during the CT scanning. The diameter of the sample is limited to 7 mm to ensure proper transmission of X-ray from the sample during CT scanning. Further, two notches are designed to help identify the end points of single tracks, which would assist during CT scanning as they are used as a reference to align the sample for CT scanning. Figure 1(b) demonstrates the alignment of the single tracks on top of the previously fabricated semicylinder. The cylinder samples contain four single tracks within, and the two neighbor tracks are formed 0.9 mm apart. This gap is needed to avoid the denuded area during the track formation [28] as well as to minimize the effect of the residual heat from one track to another.

The Ti-6Al-4 V powder with 0–45 $\mu$m powder size distribution was used to fabricate single-track samples using EOS M270 system and the layer thickness during the SLM build was 30 $\mu$m. Argon was supplied to the chamber to maintain the inert atmosphere during the build. The samples were separated from the build plate after the build was complete, and the remaining support structures were then removed by polishing. Figure 2 shows the as-build samples over the build plate and the samples after the support removal.

## 2.2 Process Parameter Design.
Pores formed in the SLM process are generally characterized as keyhole pores and lack of fusion pores [17]. Keyhole pores are formed when the vapor bubbles are trapped within the melt pool, which occurs at higher energy densities, and lack of fusion pores are formed when some regions remain unmelted as a result of lower energy density. Energy density in the SLM process is defined as [29,30]
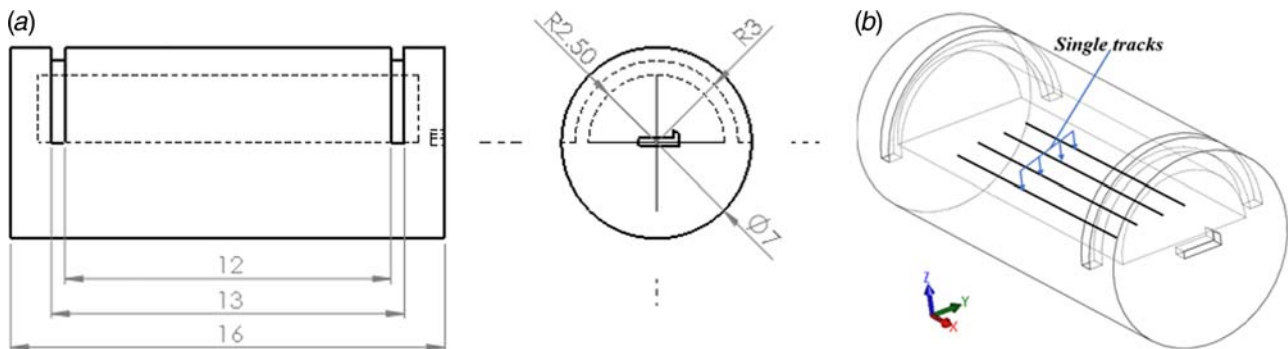
$$E = \frac{P}{v * d * t} \qquad (1)$$



**Fig. 1** (a) CAD model of the specimen (unit in mm) and (b) representation of single track designed on top of previously deposited semicylinder
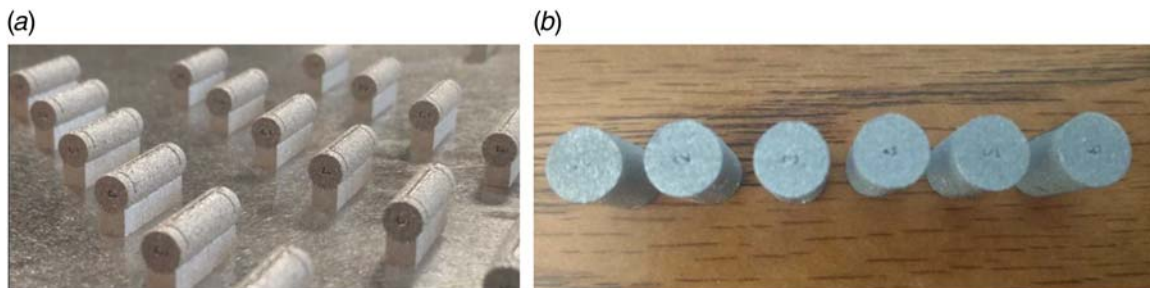


**Fig. 2** (a) Samples after removal from the machine and (b) after support removal

where $P$ is the laser power, $v$ is the scanning speed, $d$ is the hatch spacing, and $t$ is the layer thickness.

Line scanning is the foundation of the SLM process, and the combination of line scanning results in the formation of a layer. The study of single-track properties at constant layer thickness may reveal pore formation mechanisms while reducing the variables such as hatch spacing. And the line energy density (LED) can be simplified as [31]

$$LED = \frac{P}{v} \qquad (2)$$

Table 1 shows the laser power and the scan speed used in this investigation and their corresponding LED. Three replicates were fabricated to assess the repeatability of the pore formation.

LED-based studies deliver the combined effect of the power and the speed on the porosity level. Some studies claim that the use of a specific volumetric energy density would result in high-density parts [9,32]. However, the same energy density can be obtained with a different set of power and speed. And the energy density may not be the sufficient criteria to reach that conclusion as energy density is not able to capture the complex physics such as Marangoni flow, hydrodynamic instabilities, and recoil pressure, which would dictate the track morphology [33]. Therefore, it is desired to understand the effect of the power and the scan speed on the porosity. For this purpose, a different set of parameters are designed keeping the energy density as constant. Three energy densities (0.32 J/mm, 0.4 J/mm, and 0.48 J/mm) are used to investigate

the effect of the power and the scan speed on pore formation as well as overall single-track property. Table 2 presents the list of the power and the speed corresponding to the three energy densities. The maximum power of the laser (195 W) has been used for all cases, and the speed has been modified based on the energy density.

**2.3 Pore Measurement and Analysis.** CT scanning of the fabricated samples was performed using a Bruker SkyScan 1173 micro-CT scanner which has three major components: X-ray source, sample stage, and flat panel detector as shown in Fig. 3(a). The polychromatic X-ray source emits the conical beam and can generate up to 130 kV X-ray. Since the absorption of Ti-6Al-4 V is very high, the maximum voltage of 130 kV is used during the scan. However, the X-ray being polychromatic, an appropriate filter must be used to absorb low energy X-rays. 0.25 mm brass filter is used to absorb X-ray with energy below 90 kV, which in turn changes the camera sensitivity for X-ray radiation. This is necessary for highly dense materials to reduce beam hardening artifact otherwise the outer surface would appear more dense than interior due to higher absorption of low energy X-rays near the outer surface. Some of the filtered X-ray beams gets absorbed by the sample, and some penetrate through the sample which excites the camera sensor. The typical minimum transmission through the sample lies between 18% and 19%.

Radiotransparent materials like clay, Styrofoam, and parafilm tapes are used to mount the cylinder sample to the brass stage. The parafilm tape is wrapped around the sample to ensure there is no movement during the scanning. The samples were scanned using 6 $\mu$m pixel size and 2000 magnification. Rotation step of 0.1 deg was used, and 360 deg scanning was performed to obtain 3600 raw images. After obtaining raw images, steps toward reconstruction such as beam hardening correction, ring artifact reduction, misalignment compensation, and smoothing were performed using parameter fine-tuning to minimize the ring artifacts and blurring effects, etc. Reconstruction from scan projection images into cross-sectional images was carried out using NRECON, which is a software from Bruker.

CT-ANALYSER (CTAN) is also a software from Bruker, which is used for measuring quantitative parameters from scanned 3D datasets

**Table 1 Process parameters used to investigate energy density (J/mm) effect**

| Power (W) \ Speed (mm/s) | 200 | 400 | 600 | 800 | 1000 | 1200 |
|---|---|---|---|---|---|---|
| 125 | 0.63 | 0.31 | 0.21 | 0.16 | 0.13 | 0.10 |
| 150 | 0.75 | 0.38 | 0.25 | 0.19 | 0.15 | 0.13 |
| 175 | 0.88 | 0.44 | 0.29 | 0.22 | 0.18 | 0.15 |
| 195 | 0.98 | 0.49 | 0.33 | 0.24 | 0.19 | 0.16 |

**Table 2 Process parameters used to investigate power and speed effect**

| ED (J/mm) | Speed (mm/s) | 50 | 100 | 150 | 200 | 250 | 300 | 350 | 406.2 | 450 | 487.5 | 550 | 609.4 |
|---|---|---|---|---|---|---|---|---|---|---|---|---|---|
| 0.32 | Power (W) | 16 | 32 | 48 | 64 | 80 | 96 | 112 | 130 | 144 | 156 | 176 | **195** |
| 0.4 | | 20 | 40 | 60 | 80 | 100 | 120 | 140 | 162.5 | 180 | **195** | — | — |
| 0.48 | | 24 | 48 | 72 | 96 | 120 | 144 | 168 | **195** | — | — | — | — |

The bold font was used to indicate the maximum power level of the system. This limited the applicable parameter set for all line energy densities.
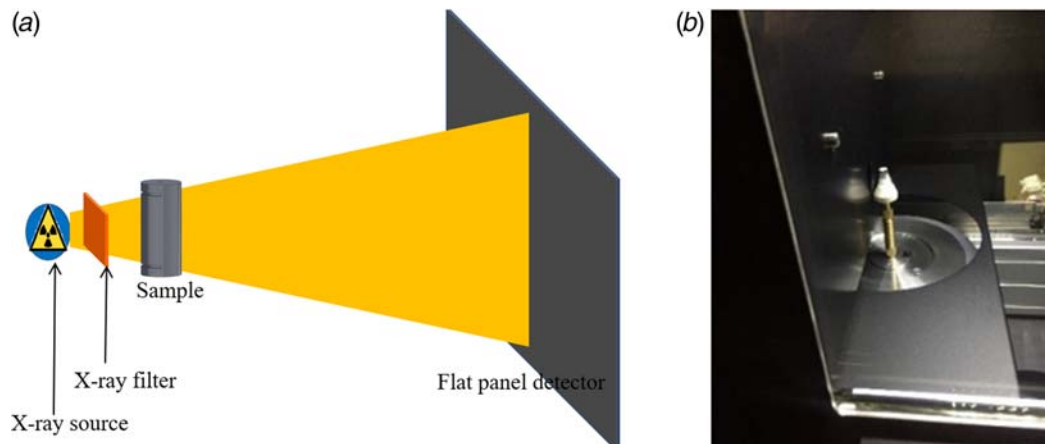


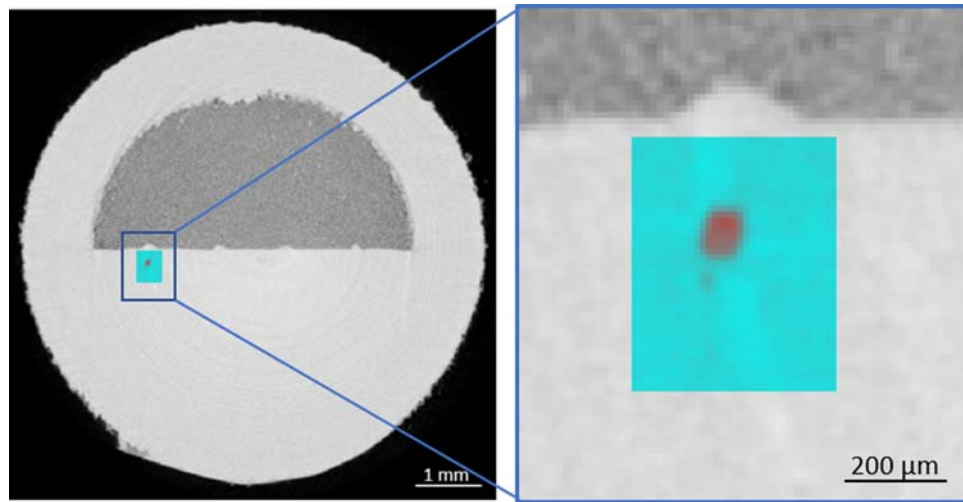Fig. 3 (a) Schematic of $\mu$CT components and (b) specimen setup in the CT system

**Fig. 4 Selection of region of interest for porosity measurement**

obtained with SkyScan micro-CT instruments. For the measurement of keyhole pores, an individual volume of interest was generated with a transverse cross-sectional dimension of $400\,\mu m \times 500\,\mu m$, and the length of 13 mm for every single track as shown in Fig. 4. Then, the reconstructed images were converted into binary images for pore measurement. Individual pores were analyzed in geometry using CTAN software, and various pore characteristics such as the pore volume, the surface area, the sphericity, etc. were obtained as a result.

## 3 Results and Discussion

**3.1 Typical Scanning Result.** After generating a reconstructed data, DATAVIEWER software was used to observe the single track formed within the cylinder. Figure 5 exhibits the CT images from a typical specimen with different sectional views as well as the isometric partial cutoff view. The grayscale image shows the density difference between the material, the light gray area represents solid Ti-6Al-4 V, the medium gray area represents powder,
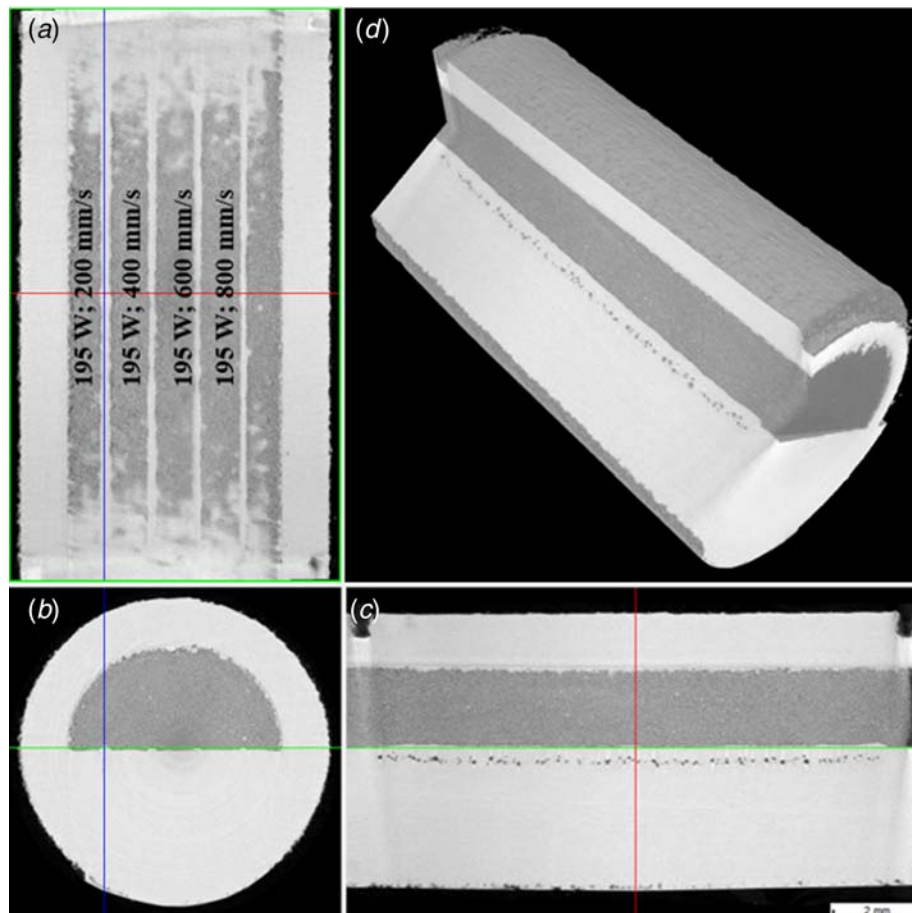


**Fig. 5 (a) Coronal (X–Z), (b) transaxial (X–Y), (c) sagittal (Z–Y) cross-sectional views, and (d) 3D partial cutoff view**
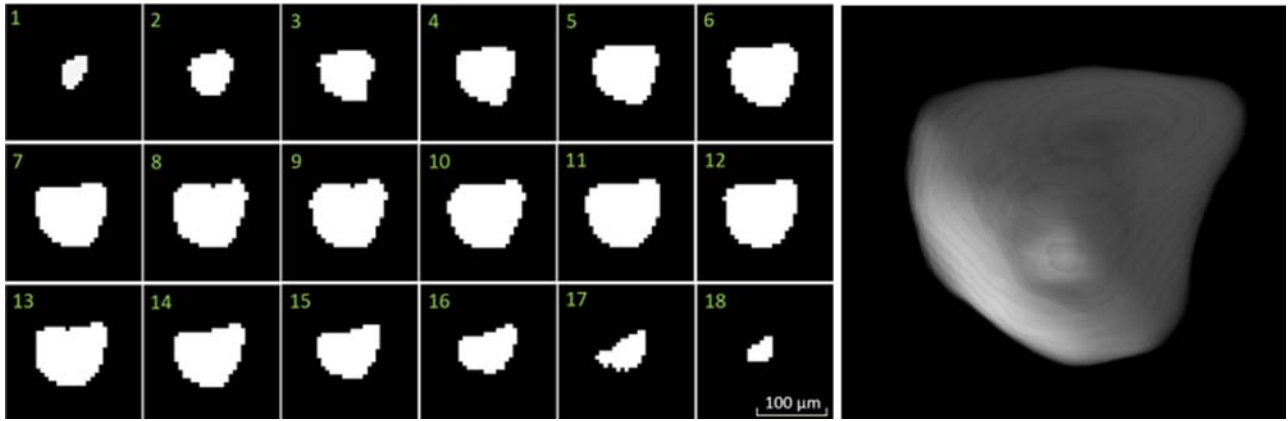
**Fig. 6  A 3D pore on right is rendered from the 2D images from the left**

and the black spots in the sagittal view, which represent the density of air, are pores. Four single tracks shown in the figure were formed with 195 W power at scan speeds of 200 mm/s, 400 mm/s, 600 mm/s, and 800 mm/s. The sagittal cross-sectional image, obtained from the center of 195 W and 200 mm/s track, clearly shows the pores formed within the single track. Besides the single track, the other solid regions were formed with the power of 170 W, a scan speed of 1200 mm/s, and hatch spacing of 100 $\mu$m.

**3.2 Pore Characteristics.** Pore characteristics are obtained from the morphometry analysis of the binary images. In CTAN, the binarization of the images is done by thresholding, which transforms the grayscale images into binary images. The binarized images have been shown in Fig. 6, where the white pixels represent the pore and the black pixels represent the solid Ti-6Al-4 V. Individual pore analysis is then performed to obtain the pore information such as pore volume, pore surface area, sphericity, etc. 3D pores are rendered from the series of 2D images. Figure 6 presents an illustration of how the 18 successive images are used to form a 3D pore.

Sphericity can be used to characterize and differentiate between pores formed due to low energy density and high energy density [17]. Sphericity ($\psi$) is a measure of how close a body is to the mathematically perfect sphere, which can be calculated by using the relationship

$$\psi = \frac{\pi^{1/3} (6V_p)^{2/3}}{A_p} \tag{3}$$

where $V_p$ is the volume of the pore and $A_p$ is the surface area. Pores formed due to lower energy density may be significant during a layer formation or multilayer scanning as the pores are formed due to partial melting. However, during the single-track formation, only keyhole pores are identified, and the discontinuity observed due to lower energy density have not been considered as pores. Figure 7(a) shows the reference point used to measure the pore locations. The locations of the pores are measured from the beginning of the scan track (X), the deviation of the pore from the middle of the track (Y), and the depth of pore centroid from the substrate free surface over which a single track is formed (Z). Figure 7(b) shows 12 pores formed at the end of a single track created with parameters 195 W and 400 mm/s (0.49 J/mm), and Table 3 shows the detailed characteristics of those pores. The sphericity of all the pores is above 0.8, which mean that they have a nearly spherical shape [17]. These are the pores formed due to very high energy input, and the pores are formed up to 200 $\mu$m deep which indicated that the pores are the result of deep penetration melting. In addition, the pore centroids formed due to keyhole mode melting are located very close to the center of the laser beam.

**3.3 Process Effects.** It has been recognized that laser power and scan speed would affect the single-track property. The mode of melting during the single-track formation depend upon these parameters and the metallographic studies showed that at high line energy densities keyholes pores are formed [34]. But the number of pores formed at different LEDs is unknown. Therefore, this study aims to find the relationship between the energy density and the keyhole porosity. Besides keyhole pores, pores may also
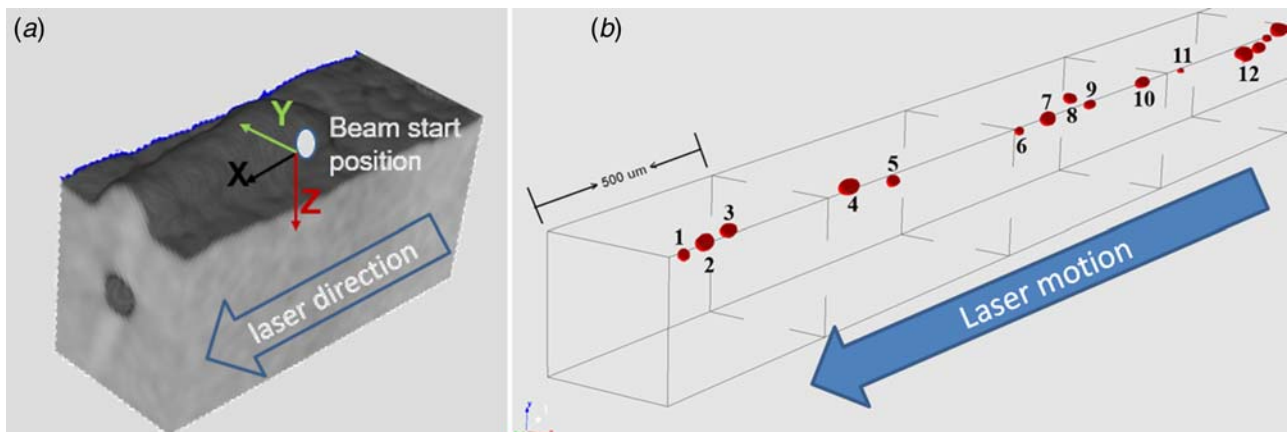


**Fig. 7  (a) Pore location definition and (b) detailed view of pores formed at the end of scan track from 195 W 400 mm/s parameters (0.49 J/mm)**

**Table 3  Location and properties of 9 pores from 195 W and 400 mm/s (0.49 J/mm)**

| Pore ID | Volume $\times 10^5$ ($\mu m^3$) | Equivalent diameter ($\mu m$) | Sphericity | $X \times 10^4$ ($\mu m$) | $Y$ ($\mu m$) | $Z \times 10^2$ ($\mu m$) |
|---|---|---|---|---|---|---|
| 1 | 1.38 | 29.7 | 0.89 | 1.17 | 1.34 | 2.02 |
| 2 | 3.96 | 42.3 | 0.88 | 1.15 | −3.33 | 1.88 |
| 3 | 3.15 | 39.2 | 0.89 | 1.14 | −3.29 | 1.84 |
| 4 | 7.11 | 51.4 | 0.89 | 1.09 | 6.04 | 1.58 |
| 5 | 1.60 | 31.3 | 0.82 | 1.06 | −3.72 | 1.81 |
| 6 | 1.02 | 26.9 | 0.95 | 0.98 | −16.9 | 1.70 |
| 7 | 4.18 | 43.1 | 0.90 | 0.97 | 1.9 | 1.61 |
| 8 | 2.87 | 38.0 | 0.89 | 0.96 | −2.49 | 1.16 |
| 9 | 1.97 | 33.5 | 0.88 | 0.94 | 4.81 | 1.53 |
| 10 | 3.64 | 41.1 | 0.9 | 0.91 | 14.5 | 1.45 |
| 11 | 0.25 | 16.9 | 0.84 | 0.88 | 17.5 | 1.42 |
| 12 | 9.47 | 56.5 | 0.87 | 0.82 | −10.2 | 1.78 |

form at the end of the track due to the collapse of the depression upon turning the laser off [35]. Hence, a wide range of LEDs has been selected to investigate the pore formation, and the results are explained in Sec. 3.3.1.

In the laser melting process, power is the most significant parameter while determining the penetration depth [36], while laser speed is a significant factor toward the width of the heat affected zone [37]. The behavior of the melt pool would change with changes in the laser power and the scan speed. As the LED does not correspond to the unique laser power and scan speed, it may not be used as an individual parameter to define the optimal processing condition. For the same LED, the level of porosity may change depending upon the combination of the laser power and the scan speed. Hence, it becomes important to inquire about the effect of different levels of power and speed within the same LED toward porosity. Section 3.3.2 explains the effect of the power and speed on the porosity within the same LEDs.

*3.3.1  Line Energy Density Effect.* The energy density, e.g., LED in single tracks determine how much energy per unit length is being supplied to the powder bed system. Thus, the peak temperature of the melt pool as well as the magnitude of depression will change. As a result, the melt pool length, width, and depth will depend on the LED. Figure 8 shows the single-track morphology obtained from different LEDs. The results indicated that the track width is proportional to the LED. As the energy density increased, the track width increased. For the same power, the amount of heat input per unit area increases as the scanning speed decreases. The
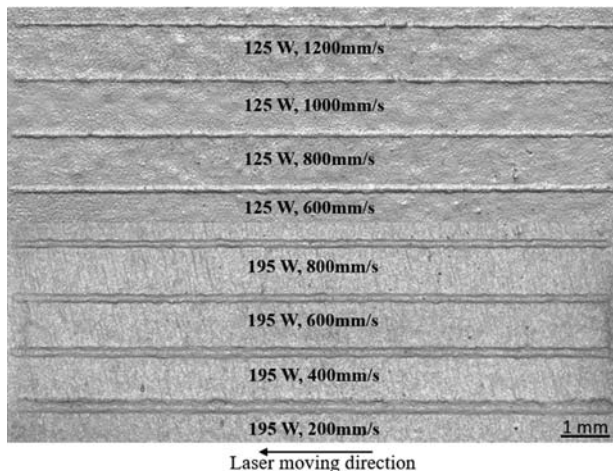


Fig. 8  Single-track morphology from different energy densities

investigated parameters formed a dense track, and no balling behavior was observed. However, for 125 W, 1200 mm/s discontinuity in the track was observed at certain locations. This may fall within the transition region between conduction mode melting and incomplete melting.

Figure 9 presents the 3D rendered pores and their location along the single tracks for three cases: 195 W and 200 mm/s (0.98 J/mm), 195 W and 400 mm/s (0.49 J/mm), and 195 W and 600 mm/s (0.33 J/mm). The frequency of the pore decreased with increasing scan speed for the same power level. Pores during deep penetration melting are formed due to keyhole instability [38], and the reduction in pore count may indicate that the severity of keyhole fluctuation is reduced with decreasing energy density. In addition, only 4 pores were observed for 195 W and 600 mm/s compared with 41 pores for 195 W and 400 mm/s. This difference may be due to the transition from keyhole mode melting to conduction mode melting. Among the four pores observed for 195 W and 400 mm/s case, one pore formed at the end of the track was significantly larger than the other three. The pores at the end of the tracks are observed in other low energy density cases as well. When the laser turns off at the end of the single track, the melt pool flows to fill the depression formed during the laser scanning. However, due to rapid solidification, the melt flow may not be able to fill the depression, especially when the depression is deeper as a result of which the pores are formed [35].
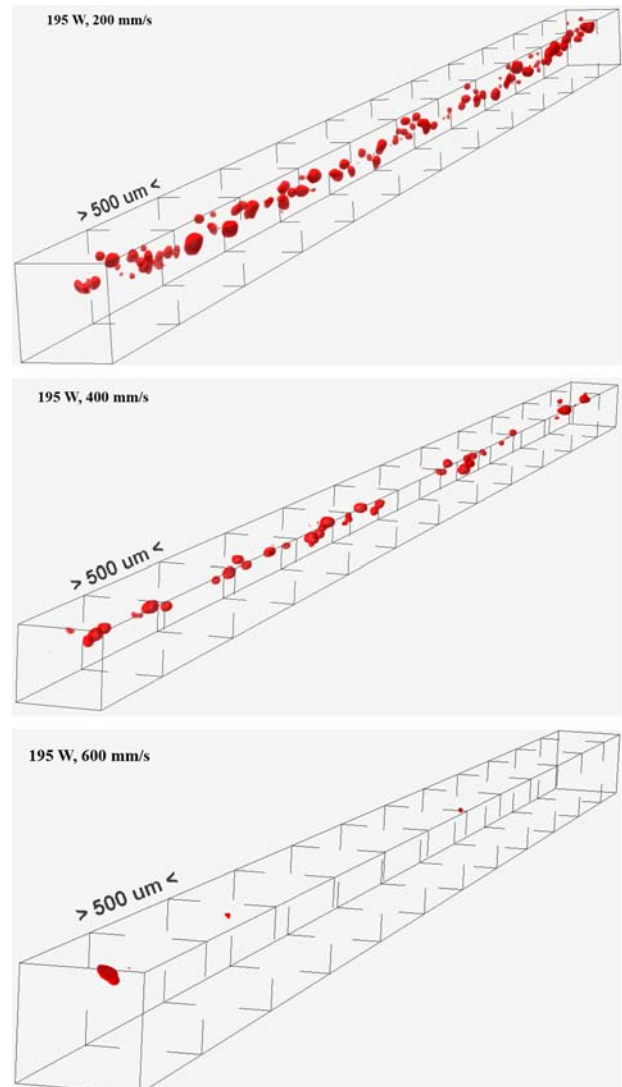


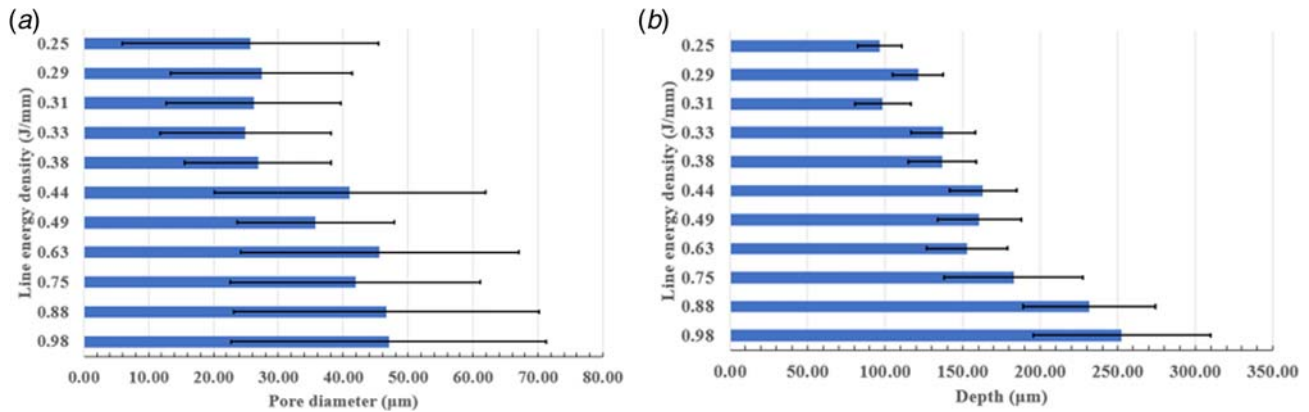Fig. 9  3D pore view observed at different process parameters

**Fig. 10 (a) Pore diameter and (b) pore depth summary from different LEDs**

Figure 10 shows the average diameter and depth of the pores formed with different LEDs. The standard deviation shown in the error bar indicated that there is a huge variation in the size of the pores formed within the same single track compared with the depth of the pores. In general, as the energy density increased, the average pore diameter and depth increased. High energy density would increase the melt pool temperature due to which material evaporation occurs leading to the formation of a vapor column. As the absorptivity of the melt pool increases with the formation of a vapor column, keyhole depth is also increased [39]. The size of the vapor column depends on the applied intensity, and the collapse of bigger vapor column may lead to larger pores while the collapse of narrower vapor column may lead to smaller pores. For the highest energy density of 0.98 J/mm, average pore depth is 252.5 $\mu$m. The average diameter of the pores formed as a result was 47 $\mu$m, with the range from 8 $\mu$m pore to 127 $\mu$m.

The pores are formed at different depths with different process parameters. It is difficult to explain the melt pool depth resulted from different power level with the study of porosity alone. However, the pore depth would provide an insight on how deep the keyhole penetration is as the metallurgical studies show that keyhole pores are mostly formed at the bottom of the melt pool [20,34]. And the keyhole penetration increased with increasing energy density. Besides, another study also showed that for the same speed, increasing the laser power would increase the keyhole depth which may induce more keyhole pores [40].

Figure 11 summarizes the average pore volume and the number of pores formed from the single tracks with 24 different energy densities. The averages were taken from three replicates, and the error bar shows the minimum and the maximum pore number and pore volume obtained from three replicates. The keyhole porosity decreased with decreasing energy density as the magnitude of the keyhole effect decreased. Among the investigated energy densities, the maximum average number of pores and volumes were observed for 0.88 J/mm (195 W and 400 mm/s). The pore number is obviously higher for 0.88 J/mm compared with 0.98 J/mm (195 W and 200 mm/s); however, the range in pore volume showed no clear difference between these two energy densities. Nonetheless, the energy densities with the power of 175 W (0.44 J/mm with 400 mm/s and 0.29 J/mm with 600 mm/s) resulted in higher number as well as volume of pores compared with the power of 195 W with respective scan speeds (0.49 J/mm with 400 mm/s and 0.33 J/mm with 600 mm/s). These results influenced the study of power and speed effect toward keyhole porosity.

The results are further interpreted based on the power and the speed in Fig. 12. A plot has been generated to identify the variation in average pore volume within the same scan speed. The trend of porosity is repeated, as for the same power, the porosity level decreased with increasing scanning speed. In addition, for the same speed, increasing the power would increase the pore volume with an exception from 175 W to 195 W, which may have some relationship with the keyhole depth and its stability.

After analyzing the energy density effect on porosity, it was observed that the pore number and pore volume generally increased with increasing energy density. However, there is a significant drop in pore number and pore volume when LED increased from 0.31 J/mm to 0.33 J/mm and 0.44 J/mm to 0.49 J/mm. In addition, the average pore number and pore volume also decreased when LED increased from 0.88 J/mm to 0.98 J/mm. The energy densities where the drop in the porosity occurred had the same power of
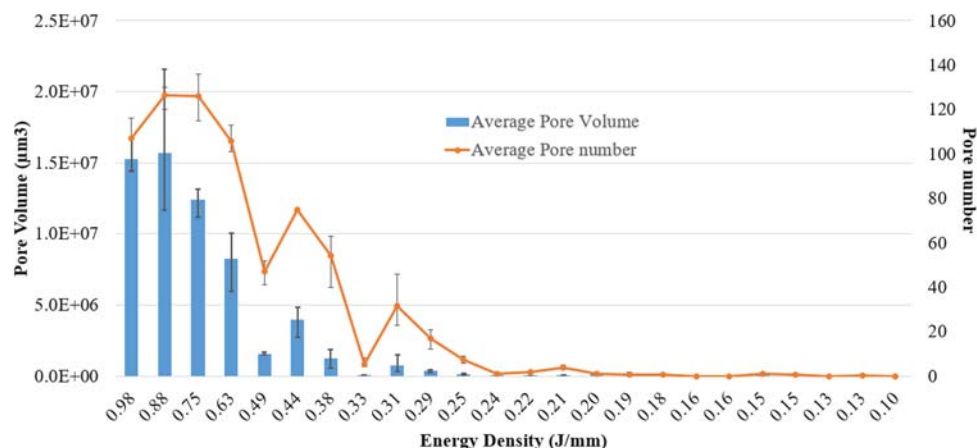


**Fig. 11 Total pore volume corresponding to different energy densities used**
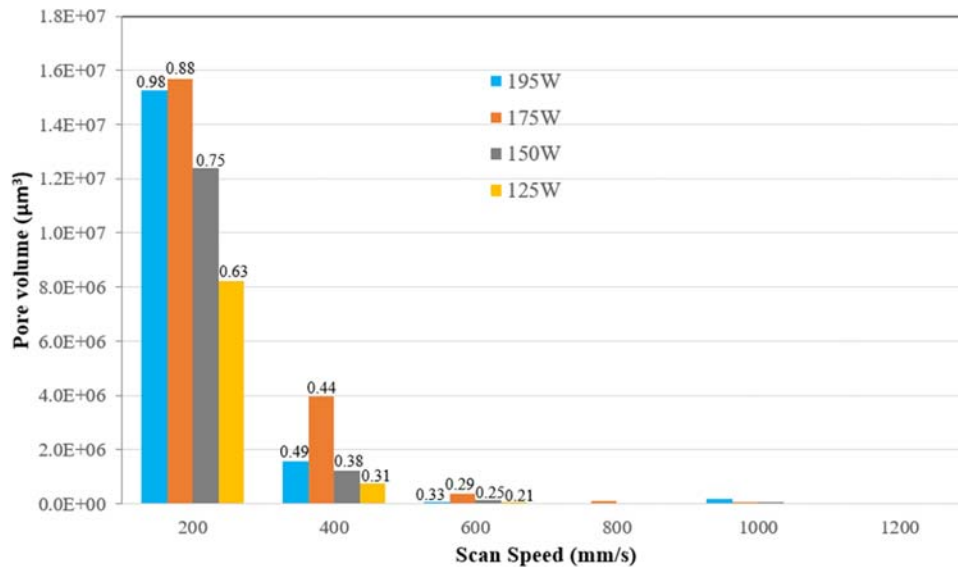
**Fig. 12  Average pore volume at different power and speed**

195 W. These results suggest that energy density may not be enough criterion to determine the porosity level, as power seems to contribute more towards porosity. Moreover, it has been reported that the volumetric energy density is not an appropriate metric to quantify melt pool depth [33], which may also contribute toward porosity. Hence, individual effects of power and speed of the same energy have been investigated.

### 3.3.2 Effect of Power and Speed at the Same Energy Density.
Based on the LED effect study, three energy densities which resulted in the keyhole pores have been selected to study the effect of the power and the speed within the LEDs. The single-track morphologies obtained from a different combination of laser power and scan speed (LED = 0.48 J/mm) have been presented in Fig. 13(a). The average widths from all the tracks were measured, and the range of the track width and the averages have been summarized in Fig. 13(b). The track morphology shows that when the power level is low, a discontinuous track is formed even at a higher energy density. This behavior is like that of the low energy density cases of an incomplete melting regime. When a low power is used, the applied energy is not enough to form a fully developed melt pool, and partial melting leads to the balling formation. The balling formation at the high energy density but

low power and scan speed may be explained based on the temperature of the melt pool. The peak temperature within the melt pool for a beam moving with a speed $v$ is [20]

$$T_{max} = \frac{\sqrt{2}AI\sigma}{k\sqrt{\pi}} \tan^{-1} \sqrt{\frac{2D}{v\sigma}} \qquad (4)$$

where $A$ is the absorptivity, $\sigma$ is the half width of Gaussian beam at the surface, $I$ is the laser intensity which is related to the laser power ($P$) as $I = P/2\pi\sigma^2$, $D$ is the thermal diffusivity of the molten material, and $k$ is the thermal conductivity. Based on the analytical expression presented in Eq. (4), the peak temperature to a great extent depends on the laser power rather than scan speed. Hence, lowering the laser power within the same energy density would mean lowering the melt pool temperature. If the power is too low, partial melting may occur like that in 24 W and 50 mm/s case. Such discontinuous tracks are observed for lower power cases in other energy densities as well: 16 W and 50 mm/s and 32 W and 100 mm/s for 0.32 J/mm and 20 W and 50 mm/s for 0.4 J/mm energy densities.

As the power and speed was increased, it resulted in the formation of continuous and wider tracks. 48 W laser power with 100 mm/s speed only resulted in an average track width of 146 $\mu m$, whereas track width beyond this power and speed were
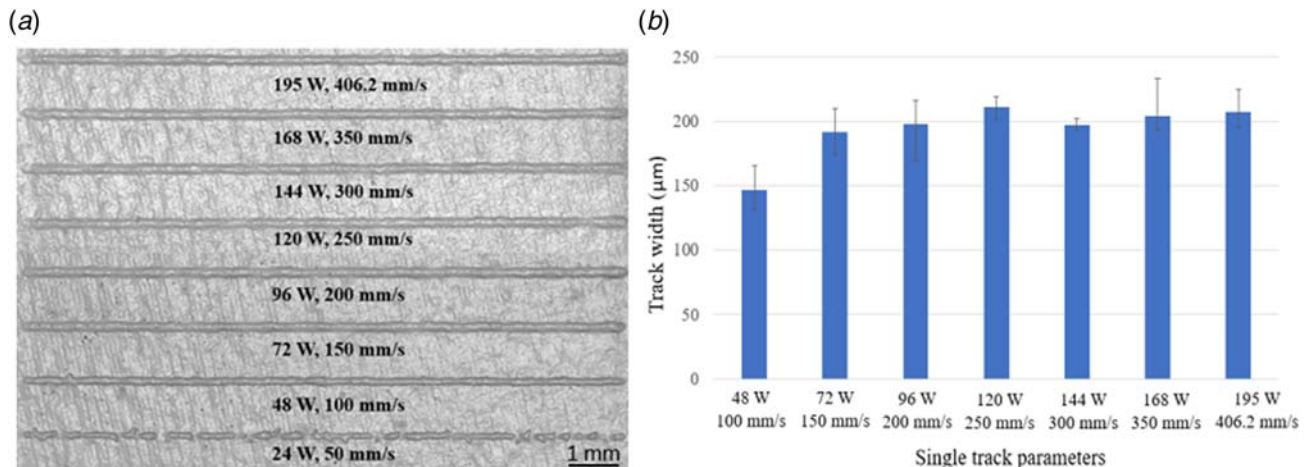


**Fig. 13  (a) Single-track morphology and (b) track widths at different process parameters for LED = 0.48 J/mm**
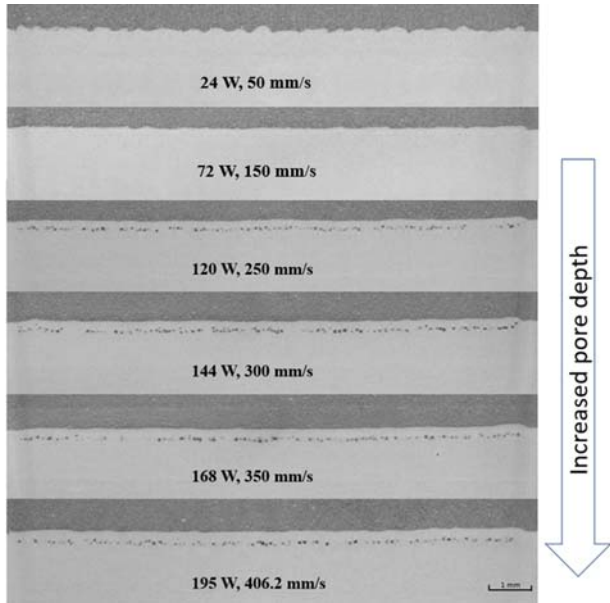
**Fig. 14  Longitudinal sections from the single tracks with ED = 0.48 J/mm**

over 190 $\mu$m. The melt pool width remained indifferent with further increase in the power and the speed. This may be due to the keyhole mode melting as the flow became dominant along the depth which resulted in almost a similar track width.

The longitudinal cross sections of the single tracks for 0.48 J/mm LED have been presented in Fig. 14. The longitudinal section of the single track with 24 W and 50 mm/s shows wavy profile due to discontinuity in the track. As the power and speed were increased, the waviness was reduced, and continuous, dense tracks were formed. Single tracks with 48 W and 72 W did not reveal pores, while as the power increased beyond 72 W, numerous pores were observed. Furthermore, the average depth of the pores increased with an increase in power as shown in Fig. 15(b). Pore depth has a lower deviation compared with the pore diameter within the same track. The results show that the characteristics of the keyhole highly depend on the level of power.

The increase in pore depth with an increase in power within the same energy density may be explained with the nondimensional depth during laser melting. It has been shown that in the laser welding, the nondimensional depth of the weld ($\delta^*$), which is the ratio of depth to the beam diameter, is related to the laser parameters and material properties by the expression [41]

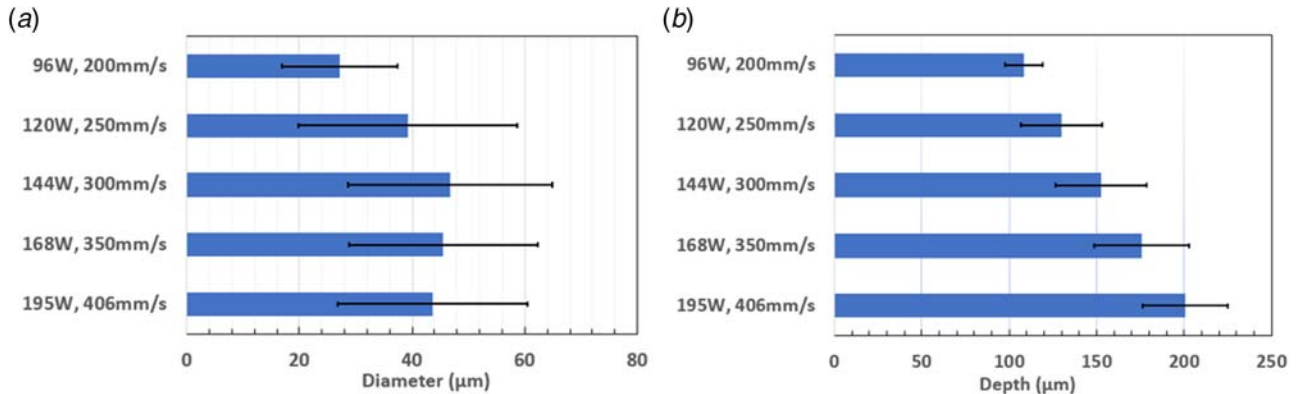$$\delta^* = fn\left(\frac{ACP}{\rho h_s \sqrt{Dv\sigma^3}}\right) \qquad (5)$$

where $C$ is a constant with no dimensions and $h_s$ is the enthalpy at melting. From Eq. (5), it is apparent that the power has more effect on the depth of the melt pool.

Figure 16 presents the summary of the effect of the power and the scan speed on the pore count and the pore volume. The average pore number and pore volume along with their range obtained from three replicates are presented. It is observed that the level of porosity increased with increasing energy density for the same level of power. In addition, as the power and speed increased for the same energy density, the pore count and the total pore volume increased. As the power would affect the keyhole depth, pore count and volume may increase with increasing power. However, this was not always true for the same energy density as increasing power after a certain level decreased the pore number as well as pore volume. In addition, power appeared to be more significant toward the pore volume as the critical power seems to be similar for all three cases. At low power and low speed, no or very few pores were observed. The pore count increased significantly around the power of 100 W and continued to increase until 140 W. For 0.32 J/mm LED, the average maximum volume of the pore was observed at 130 W. However, for 0.4 J/mm and 0.48 J/mm, the maximum number and volume of pores formed at 140 W and 144 W, respectively. As the power was further increased, the total pore volume decreased while the depth of the pores increased.

The observed results in Fig. 16 may be explained with the help of Fig. 17, which shows the relationship between the excess pressure due to evaporation (($p + p_o$)/$p_o$) and the surface tension pressure, depending upon the normalized keyhole radius $a/\sigma$ [42]. The pressure on the keyhole wall ($p + p_o$) is normalized with an ambient pressure $p_o$, and the keyhole radius ($a$) is normalized with laser beam radius $\sigma$.

Equations (6) and (7) show the energy balance and pressure balance equations, which can be solved numerically to obtain equilibrium keyhole radius [42]. The energy balance equation is

$$q_{abs} = q_\lambda + q_{abl} \qquad (6)$$

where $q_{abs}$ is the absorbed energy flux density, $q_\lambda$ is the heat conduction losses, and $q_{abl}$ is the energy carried away by evaporation. And the pressure balance equation is

$$p_{abl}(a) = p_\Upsilon(a) \qquad (7)$$

where $p_{abl}(a)$ is the evaporation pressure and $p_\Upsilon(a)$ is the surface tension pressure. Based on these, there exist two equilibrium states as shown in Fig. 17: point A and point B. Point A is called an unstable equilibrium as the surface tension exceeds evaporation pressure to its left which leads to collapsing keyhole, while to the right, evaporation pressure exceeds the surface tension pressure and keyhole will expand to the equilibrium state B. Furthermore, five different evaporation pressure curves are shown for different absorbed laser power per thickness ($P_{abs}/d$). It shows that there



**Fig. 15  Pore diameter and pore depth summary from process parameters of LED = 0.48 J/mm**
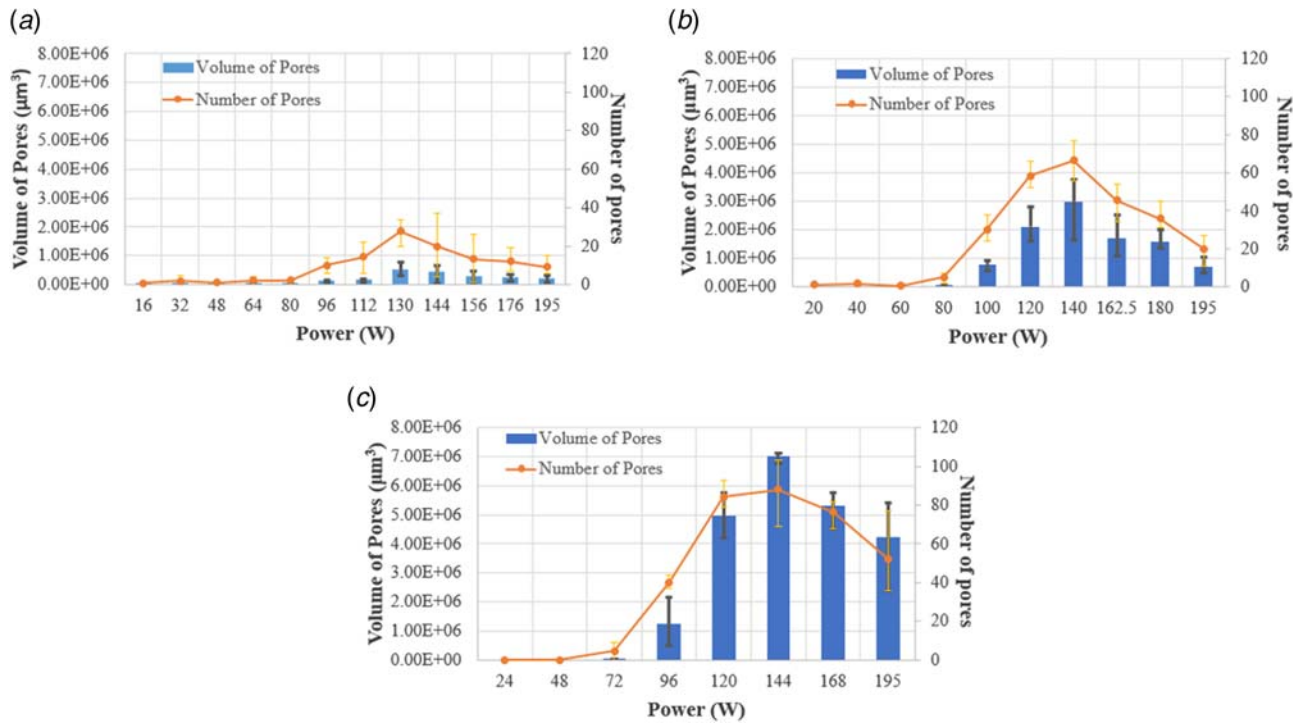
**Fig. 16 Pore count and pore volume obtained at different process parameters from different energy densities (a) 0.32 J/mm, (b) 0.4 J/mm, and (c) 0.48 J/mm**
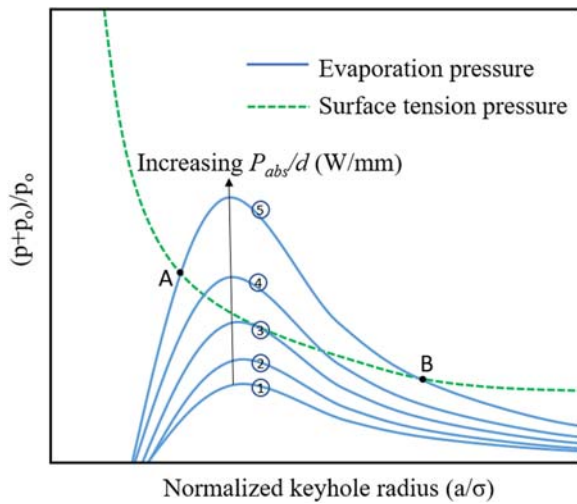


**Fig. 17 Stability of keyhole formation affected the evaporation pressure and the pressure due to surface tension at different energy densities [42]**

exists a threshold value of the absorbed laser power per thickness (curve 3) below which a keyhole cannot exist. This would explain the formation of keyhole pores at higher power and speed and incomplete melting at lower power and speed, which has been shown in Fig. 14. That is, for the same energy density, when the power and speed keep on increasing, the melting mode changes from partial melting to conduction melting to keyhole melting. In addition, the probability of pore formation increases around unstable equilibrium, and as the keyhole diameter further increases with an increase in power, the keyhole melting is stable, and the probability of pore formation decreases. This may be the reason for the trend observed in Fig. 16. As the power was increased to around 140 W, the unstable equilibrium was reached, and with a

further increase in power, the keyhole became more stable thus reducing the number and volume of pores.

## 4 Conclusions

In this study, laser single-track scanning was conducted using an EOS M270 and Ti-6Al-4 V powder with different parameters, total 24 different LEDs, ranging from 0.1 J/mm to 0.98 J/mm, to investigate the relationship between the porosity severity and the LED. Keyhole pores formed in the single tracks were measured using a SkyScan 1173 micro-CT scanner, followed by data analysis to obtain individual pore geometry and the overall characteristics such as the pore volume, the pore depth, the sphericity, etc. Moreover, to investigate the laser power effect under the same energy density on the keyhole porosity, three energy LED levels, 0.32 J/mm, 0.4 J/mm, and 0.48 J/mm, were tested with a wide range of laser powers. The results and analyses lead to the following conclusions.

(1) At the same LED, increasing the laser power shows a distinct transition from incomplete melting to conduction melting, and to keyhole melting. Considering 0.48 J/mm, at a low power level (24 W and 50 mm/s), balling formation due to incomplete melting is observed. On the other hand, as the power increases from 96 W to 195 W, keyhole pores are observed, and the depth of the pores increases with increasing the laser power.

(2) Keyhole porosity generally increases with increasing the LED. However, it is observed that the porosity decreases when the LED increases from 0.31 J/mm to 0.33 J/mm, from 0.44 J/mm to 0.49 J/mm, and from 0.88 J/mm to 0.98 J/mm.

(3) For the pore size, the equivalent pore diameters measured are in a wide range, from 8 $\mu$m to 127 $\mu$m and the frequency of larger pores appears higher in higher LEDs, which show increased average pore diameters. In addition, the pores are deeper from the surface with the increase of LED.

(4) The power/speed effect study shows that the level of the laser power is highly influential toward the keyhole porosity due to its influence on the keyhole stability. For the same LED, e.g., 0.40 J/mm, the pore number and the pore volume increase with increasing the power until about 140 W and then both the pore number and volume decrease, if the power is further increased. This may be due to the stability of the keyhole formation at different laser energy intensities.

## Funding Data

## References

[1] Kruth, J.-P., Froyen, L., Van Vaerenbergh, J., Mercelis, P., Rombouts, M., and Lauwers, B., 2004, "Selective Laser Melting of Iron-Based Powder," J. Mater. Process. Technol., **149**(1), pp. 616–622.

[2] Aboulkhair, N. T., Maskery, I., Tuck, C., Ashcroft, I., and Everitt, N. M., 2016, "On the Formation of AlSi10Mg Single Tracks and Layers in Selective Laser Melting: Microstructure and Nano-Mechanical Properties," J. Mater. Process. Technol., **230**(2016), pp. 88–98.

[3] Brandl, E., Heckenberger, U., Holzinger, V., and Buchbinder, D., 2012, "Additive Manufactured AlSi10Mg Samples Using Selective Laser Melting (SLM): Microstructure, High Cycle Fatigue, and Fracture Behavior," Mater. Des., **34**(2012), pp. 159–169.

[4] Amato, K., Gaytan, S., Murr, L., Martinez, E., Shindo, P., Hernandez, J., Collins, S., and Medina, F., 2012, "Microstructures and Mechanical Behavior of Inconel 718 Fabricated by Selective Laser Melting," Acta Mater., **60**(5), pp. 2229–2239.

[5] Jia, Q., and Gu, D., 2014, "Selective Laser Melting Additive Manufactured Inconel 718 Superalloy Parts: High-Temperature Oxidation Property and its Mechanisms," Opt. Laser Technol., **62**(2014), pp. 161–171.

[6] Rafi, H., Karthik, N., Gong, H., Starr, T. L., and Stucker, B. E., 2013, "Microstructures and Mechanical Properties of Ti6Al4 V Parts Fabricated by Selective Laser Melting and Electron Beam Melting," J. Mater. Eng. Perform., **22**(12), pp. 3872–3883.

[7] Song, B., Dong, S., Zhang, B., Liao, H., and Coddet, C., 2012, "Effects of Processing Parameters on Microstructure and Mechanical Property of Selective Laser Melted Ti6Al4 V," Mater. Des., **35**(2012), pp. 120–125.

[8] Guan, K., Wang, Z., Gao, M., Li, X., and Zeng, X., 2013, "Effects of Processing Parameters on Tensile Properties of Selective Laser Melted 304 Stainless Steel," Mater. Des., **50**(2013), pp. 581–586.

[9] Cherry, J., Davies, H., Mehmood, S., Lavery, N., Brown, S., and Sienz, J., 2015, "Investigation Into the Effect of Process Parameters on Microstructural and Physical Properties of 316L Stainless Steel Parts by Selective Laser Melting," Int. J. Adv. Manuf. Technol., **76**(5–8), pp. 869–879.

[10] Edwards, P., and Ramulu, M., 2014, "Fatigue Performance Evaluation of Selective Laser Melted Ti-6Al-4 V," Mater. Sci. Eng. A, **598**(2014), pp. 327–337.

[11] Vandenbroucke, B., and Kruth, J.-P., 2007, "Selective Laser Melting of Biocompatible Metals for Rapid Manufacturing of Medical Parts," Rapid Prototyping J., **13**(4), pp. 196–203.

[12] Murr, L., Quinones, S., Gaytan, S., Lopez, M., Rodela, A., Martinez, E., Hernandez, D., Martinez, E., Medina, F., and Wicker, R., 2009, "Microstructure and Mechanical Behavior of Ti-6Al-4 V Produced by Rapid-Layer Manufacturing, for Biomedical Applications," J. Mech. Behav. Biomed. Mater., **2**(1), pp. 20–32.

[13] Yadroitsev, I., Krakhmalev, P., and Yadroitsava, I., 2014, "Selective Laser Melting of Ti6Al4 V Alloy for Biomedical Applications: Temperature Monitoring and Microstructural Evolution," J. Alloys Compd., **583**(2014), pp. 404–409.

[14] Wycisk, E., Emmelmann, C., Siddique, S., and Walther, F., 2013, "High Cycle Fatigue (HCF) [Q7]Performance of Ti-6Al-4 V Alloy Processed by Selective Laser Melting," Proc. Adv. Mater. Res. Trans. Tech. Publ., **816–817**(2013), pp. 134–139.

[15] Mercelis, P., and Kruth, J.-P., 2006, "Residual Stresses in Selective Laser Sintering and Selective Laser Melting," Rapid Prototyping J., **12**(5), pp. 254–265.

[16] Cheng, B., Shrestha, S., and Chou, Y. K., "Stress and Deformation Evaluations of Scanning Strategy Effect in Selective Laser Melting," Proceedings of the ASME 2016 11th International Manufacturing Science and Engineering Conference, Blacksburg, VA, June 27–July 1, American Society of Mechanical Engineers, p. V003T008A009.

[17] Kasperovich, G., Haubrich, J., Gussone, J., and Requena, G., 2016, "Correlation Between Porosity and Processing Parameters in TiAl6V4 Produced by Selective Laser Melting," Mater. Des., **105**(2016), pp. 160–170.

[18] Leuders, S., Thöne, M., Riemer, A., Niendorf, T., Tröster, T., Richard, H., and Maier, H., 2013, "On the Mechanical Behaviour of Titanium Alloy TiAl6V4 Manufactured by Selective Laser Melting: Fatigue Resistance and Crack Growth Performance," Int. J. Fatigue, **48**(2013), pp. 300–307.

[19] Gong, H., Rafi, K., Gu, H., Starr, T., and Stucker, B., 2014, "Analysis of Defect Generation in Ti-6Al-4 V Parts Made Using Powder Bed Fusion Additive Manufacturing Processes," Add. Manuf., **1**(2014), pp. 87–98.

[20] King, W. E., Barth, H. D., Castillo, V. M., Gallegos, G. F., Gibbs, J. W., Hahn, D. E., Kamath, C., and Rubenchik, A. M., 2014, "Observation of Keyhole-Mode Laser Melting in Laser Powder-Bed Fusion Additive Manufacturing," J. Mater. Process. Technol., **214**(12), pp. 2915–2925.

[21] Ponnusamy, P., Masood, S., Ruan, D., Palanisamy, S., and Mohamed, O., 2017, "Statistical Analysis of Porosity of 17-4PH Alloy Processed by Selective Laser Melting," Proceedings of the IOP Conference Series: Materials Science and Engineering, Beijing, China, June 23–25, IOP Publishing, p. 012001.

[22] Slotwinski, J. A., Garboczi, E. J., and Hebenstreit, K. M., 2014, "Porosity Measurements and Analysis for Metal Additive Manufacturing Process Control," J. Res. Natl. Inst. Stand. Technol., **119**(2014), pp. 494.

[23] Zhou, X., Wang, D., Liu, X., Zhang, D., Qu, S., Ma, J., London, G., Shen, Z., and Liu, W., 2015, "3D-Imaging of Selective Laser Melting Defects in a Co–Cr–Mo Alloy by Synchrotron Radiation Micro-CT," Acta Mater., **98**(2013), pp. 1–16.

[24] Ziółkowski, G., Chlebus, E., Szymczyk, P., and Kurzac, J., 2014, "Application of X-Ray CT Method for Discontinuity and Porosity Detection in 316L Stainless Steel Parts Produced With SLM Technology," Arch. Civ. Mech. Eng., **14**(4), pp. 608–614.

[25] Siddique, S., Imran, M., Rauer, M., Kaloudis, M., Wycisk, E., Emmelmann, C., and Walther, F., 2015, "Computed Tomography for Characterization of Fatigue Performance of Selective Laser Melted Parts," Mater. Des., **83**(2015), pp. 661–669.

[26] Kim, T. B., Yue, S., Zhang, Z., Jones, E., Jones, J. R., and Lee, P. D., 2014, "Additive Manufactured Porous Titanium Structures: Through-Process Quantification of Pore and Strut Networks," J. Mater. Process. Technol., **214**(11), pp. 2706–2715.

[27] Van Bael, S., Kerckhofs, G., Moesen, M., Pyka, G., Schrooten, J., and Kruth, J.-P., 2011, "Micro-CT-Based Improvement of Geometrical and Mechanical Controllability of Selective Laser Melted Ti6Al4 V Porous Structures," Mater. Sci. Eng. A, **528**(24), pp. 7423–7431.

[28] Matthews, M. J., Guss, G., Khairallah, S. A., Rubenchik, A. M., Depond, P. J., and King, W. E., 2016, "Denudation of Metal Powder Layers in Laser Powder Bed Fusion Processes," Acta Mater., **114**(2016), pp. 33–42.

[29] Thijs, L., Verhaeghe, F., Craeghs, T., Van Humbeeck, J., and Kruth, J.-P., 2010, "A Study of the Microstructural Evolution During Selective Laser Melting of Ti-6Al-4 V," Acta Mater., **58**(9), pp. 3303–3312.

[30] Vrancken, B., Thijs, L., Kruth, J.-P., and Van Humbeeck, J., 2012, "Heat Treatment of Ti6Al4 V Produced by Selective Laser Melting: Microstructure and Mechanical Properties," J. Alloys Compd., **541**(2012), pp. 177–185.

[31] Yadroitsev, I., Gusarov, A., Yadroitsava, I., and Smurov, I., 2010, "Single Track Formation in Selective Laser Melting of Metal Powders," J. Mater. Process. Technol., **210**(12), pp. 1624–1631.

[32] Read, N., Wang, W., Essa, K., and Attallah, M. M., 2015, "Selective Laser Melting of AlSi10Mg Alloy: Process Optimisation and Mechanical Properties Development," Mater. Des., **65**(2015), pp. 417–424.

[33] Bertoli, U. S., Wolfer, A. J., Matthews, M. J., Delplanque, J.-P. R., and Schoenung, J. M., 2017, "On the Limitations of Volumetric Energy Density as a Design Parameter for Selective Laser Melting," Mater. Des., **113**(2017), pp. 331–340.

[34] Gong, H., Gu, H., Zeng, K., Dilip, J., Pal, D., Stucker, B., Christiansen, D., Beuth, J., and Lewandowski, J. J., 2014, "Melt Pool Characterization for Selective Laser Melting of Ti-6Al-4 V Pre-Alloyed Powder," Solid freeform fabrication, Austin TX, Aug 4.

[35] Khairallah, S. A., Anderson, A. T., Rubenchik, A., and King, W. E., 2016, "Laser Powder-Bed Fusion Additive Manufacturing: Physics of Complex Melt Flow and Formation Mechanisms of Pores, Spatter, and Denudation Zones," Acta Mater., **108**(2016), pp. 36–45.

[36] Akman, E., Demir, A., Canel, T., and Sınmazçelik, T., 2009, "Laser Welding of Ti6Al4 V Titanium Alloys," J. Mater. Process. Technol., **209**(8), pp. 3705–3713.

[37] Benyounis, K., Olabi, A., and Hashmi, M., 2005, "Effect of Laser Welding Parameters on the Heat Input and Weld-Bead Profile," J. Mater. Process. Technol., **164**(2005), pp. 978–985.

[38] Pang, S., Chen, W., and Wang, W., 2014, "A Quantitative Model of Keyhole Instability Induced Porosity in Laser Welding of Titanium Alloy," Metall. Mater. Trans. A, **45**(6), pp. 2808–2818.

[39] Cho, J.-H., and Na, S.-J., 2006, "Implementation of Real-Time Multiple Reflection and Fresnel Absorption of Laser Beam in Keyhole," J. Phys. D: Appl. Phys. **39**(24), pp. 5372.

[40] Trapp, J., Rubenchik, A. M., Guss, G., and Matthews, M. J., 2017, "In Situ Absorptivity Measurements of Metallic Powders During Laser Powder-Bed Fusion Additive Manufacturing," Appl. Mater. Today, **9**(2017), pp. 341–349.

[41] Hann, D., Iammi, J., and Folkes, J., 2011, "A Simple Methodology for Predicting Laser-Weld Properties From Material and Laser Parameters," J. Phys. D: Appl. Phys., **44**(44), p. 445401.

[42] Kroos, J., Gratzke, U., and Simon, G., 1993, "Towards a Self-Consistent Model of the Keyhole in Penetration Laser Beam Welding," J. Phys. D: Appl. Phys., **26**(3), p. 474.